Quantitative Motion Analysis of Subchromosomal Foci in Living Cells Using Four-Dimensional Microscopy

Harald Bornfleth,*# Peter Edelmann,*# Daniele Zink,§ Thomas Cremer,¶# and Christoph Cremer*#

*Institute of Applied Physics, University of Heidelberg, 69120 Heidelberg; #Interdisciplinary Center of Scientific Computing, University of Heidelberg, INF 368, 69120 Heidelberg; §Institute of Anthropology and Human Genetics, LMU Munich, 80336 Munich; and ¶Institute of Anthropology and Human Genetics, LMU Munich, 80333 Munich, Germany

ABSTRACT The motion of subchromosomal foci and of whole chromosome territories in live human cell nuclei was investigated in four-dimensional space-time images. Visualization of subchromosomal foci was achieved by incorporating Cy3-dUTP into the nuclear DNA of two different cell types after microinjection. A subsequent segregation of the labeled cell nuclei led to the presence of only a few labeled chromosome territories on a background of nonlabeled chromatin (Zink et al., 1998. *Hum. Genet.* 102:241–251). This procedure yielded many distinct signals in a given cell nucleus. Motion analysis in four-dimensional space-time images was performed using single-particle tracking and a statistical approach to the detection of a possible directional motion of foci relative to the center of mass of a chromosome territory. The accuracy of the analysis was tested using simulated data sets that closely mirrored the experimental setup and using microparticles of known size. Application of the analysis tools to experimental data showed that mutual diffusion-like movements between foci located on different chromosomes were more pronounced than inside the territories. In the time range observed, movements of individual foci could best be described by a random diffusion process. The statistical test for joint directed motion of several foci inside chromosome territories revealed that foci occasionally switched from random to directional motion inside the territories.

INTRODUCTION

Three-dimensional (3D) chromosomal structure and nuclear architecture have been a matter of intensive research over the last several years. Studies of fixed cells have revealed that chromosomes in the nucleus are organized in mutually exclusive domains, termed chromosome territories (for review see Cremer et al., 1993; Lamond and Earnshaw, 1998). The 3D and four-dimensional (4D) (i.e., space plus time) architecture of chromosome territories is not understood at present. Early and mid to late replicating focal aggregates with diameters of some 400–800 nm apparently constitute important higher order chromatin structures. These structures were first detected immunocytochemically in fixed cell nuclei after pulse labeling during S-phase with BrdU (Nakamura et al., 1986) and other halogenated thymidine analogs (CldU, IdU) (Visser et al., 1998; Zink et al., 1999, and references therein) and were termed replication sites or replication foci. Importantly, foci have an average DNA content of ~0.3–1.5 Mbp, they remain visible after the dissassemby of replication factors, and they can be observed at other interphase stages as well (Berezney et al., 1995; Sparvoli et al., 1994; Zink et al., 1998a, 1999; Jackson and Pombo, 1998). In recognition of this fact, we have used interchangeably the terms "subchromosomal focus" and "chromatin focus" to designate these structures independently of cell cycle stage and function. It is not yet known whether each chromatin focus persists as an individual entity (i.e., composed of the same DNA sequence) during subsequent cell cycles or even throughout the entire replicative and postreplicative lifespan of a cell or whether the DNA sequence composition of foci changes over time, supporting a more dynamic view of the assembly and disassembly of chromatin foci. Both views are consistent with the hypothesis that these foci play an important functional role as higher order chromatin compartments capable of assembling different sets of factors, e.g., for replication and transcription, at different time points during the cell cycle (Wei et al., 1998; Zink et al., 1998). Recently, subchromosomal foci could be directly observed as apparently persistent structures in the nuclei of living cells, after the incorporation of fluorescent nucleotides into newly synthesized DNA strands (Zink et al. 1998a). Although it is not yet formally proved that foci observed in the nuclei of fixed and living cells, respectively, are identical structures, we believe that such an identity is highly likely. Single chromosome bands in mitotic chromosomes are apparently formed by coalescing chromatin foci. Further analysis also revealed that foci of the same (early or mid to late replicating) type form different compartments in the interphase nucleus and that volumes occupied by these foci are highly exclusive (Zink et al., 1999).

Experiments in which nuclei were irradiated with UV laser beams and where DNA damage was quantified after different time intervals suggested that the arrangement of chromosome territories did not change extensively during the cell cycle (Cremer et al., 1982). Recently it has become

Received for publication 1 October 1998 and in final form 12 August 1999.

Address reprint requests to Prof. Dr. C. Cremer, Institute of Applied Physics, University of Heidelberg, Albert-Ueberle-Strasse 3-5, 69120 Heidelberg, Germany. Tel.: ++49-6221-549250; Fax: ++49-6221-549262; E-mail: cremer@popeye.aphys2.uni-heidelberg.de.

Dr. Bornfleth's present address is Division of Biomagnetism, Neurological Clinic, University of Heidelberg, INF 400, 69120 Heidelberg, Germany.

0006-3495/99/11/2871/16 $2.00

possible to observe directly dynamic processes of chromatin on submicrometer scales in the nuclei of living cells (for a review see Zink and Cremer, 1998). One experimental strategy employs the visualization of proteins that bind to specific chromosomal subregions. Visualization is based on microinjection of fluorochrome-labeled proteins or antibodies. Alternatively, cells are transfected with DNA constructs for the expression of fusion proteins involving green fluorescent protein (GFP) (Shelby et al., 1996; Robinett et al., 1996; Buchenau et al., 1997; Marshall et al., 1997). Shelby et al. (1996) observed that centromeres in human cells "were primarily stationary, although motility of individual or small groups of centromeres was occasionally observed at very slow rates of 7–10 μm/h." In contrast, Marshall et al. (1997) noted that dynamics in a time range of several minutes could be described by a constrained Brownian motion. The diffusion was confined to a volume with a radius of 0.3 μm in the nuclei of yeast, and to 0.9 μm in the nuclei of *Drosophila melanogaster*. It has been suggested that both types of motion, motility at very slow rates and constrained Brownian motion, coexist with a third type: small-scale refolding of chromosome subdomains (Zink and Cremer, 1998). For a quantitative motion analysis, the method of single-particle tracking (SPT) (Qian et al., 1991) is valuable for obtaining diffusion coefficients by internal averaging of the trajectory of a particle. However, internal averaging leads to insensitivity to a possible transition from Brownian motion to directional motion (Saxton, 1997).

With the experimental strategy described above, well-defined regions in the cell nucleus could be visualized in vivo, ranging from two signals (Marshall et al., 1997) to approximately six signals. Our present study is based on another experimental strategy that provides many signals of subchromosomal size at once and thus enables a more detailed study of the types of chromatin motion that occur. This strategy employs the fluorescence labeling of newly replicated DNA in human cell nuclei with subsequent segregation of the labeled chromosomes into daughter nuclei (Zink et al., 1998a; Manders et al., 1999). With this technique, distinct subchromosomal foci with a diameter of 400–800 nm were observed. This approach resulted in up to 25 well-defined signals in a given chromosome territory (Zink et al., 1998a). Two types of data analysis were developed and implemented. In a first approach, SPT was used to calculate the mean square displacement (MSD) of individual foci over time. From the MSDs, the apparent diffusion coefficients of subchromosomal foci in nuclei and within chromosome territories (within the observed time interval) were obtained. The resulting values were compared to diffusion coefficients calculated from simulations with stationary targets, where a signal-to-noise ratio (SNR) similar to that in the experiments was used. In addition, the motion of whole chromosome territories or subterritories within the cell nuclei was quantified.

Because many signals could be distinguished in a given chromosome territory, the type of motion of foci inside a territory could be analyzed statistically without averaging over a large number of sampling times. In this second approach, the directions of motion of foci inside territories were tested for random distribution. The test, based on earlier work by Bingham (1964), uses the direction cosines of displacement vectors to obtain a test value S_u (see Appendix). Using this technique, we observed that foci inside territories occasionally switched from random to directional motion relative to the territory center of mass. The performance of the analysis tool was tested using simulated data, showing that the test value S_u is a reliable estimator for directional motion.

MATERIALS AND METHODS

Fluorescent labeling of subchromosomal foci in vivo

The experimental procedure for visualizing subchromosomal foci in living HeLa or neuroblastoma (SH-EP N14) cells has been described in detail elsewhere (Zink et al., 1998a). The nuclei analyzed quantitatively here are a subset of those described qualitatively by Zink et al. (1998a). Briefly, human cell nuclei were microinjected with the fluorescent thymidine analog Cy3-AP3-dUTP (Amersham), which was incorporated into the newly synthesized DNA strand during S phase. Cells continued to divide and proceed with subsequent cell cycles. The fluorochrome-linked dUTP cells were recorded 2 days (neuroblastoma) or 5 days (HeLa) after labeling. This ensured that several S phases and cell divisions occurred between labeling and image acquisition, resulting in images with few labeled chromosome territories on a background of nonlabeled chromatin (cf. Fig. 1). For living cell microscopy, HeLa and neuroblastoma cells were kept in an FCS 2 chamber (Bioptechs) at 37°C. Cells were observed to continue the cell cycle, even when mounted in the FCS 2 chamber on the microscope stage.

Data acquisition and PSF measurement

Three-dimensional images were recorded using a prototype of the Zeiss LSM 5 confocal microscope equipped with a Zeiss Plan apochromate oil objective (63×, NA 1.4). A HeNe laser with $\lambda = 543$ nm and a long-pass filter (570 nm) were used for excitation and detection of Cy3 fluorescence. A voxel size of 120 nm × 120 nm × 500 nm (x, y, and z directions) was chosen. Because the optical mismatch between the cover glass (refractive index close to that of the immersion medium, $n = 1.518$) and the cell medium (Dulbecco's modified Eagle's medium (DMEM), $n = 1.33$) led to a focal shift (Hell et al., 1993), a resulting voxel size of 440 nm (z direction) was assumed according to the results of Sheppard and Török (1997). The laser excitation intensity was reduced to a minimum to avoid photobleaching and phototoxic effects on the cells under observation. The number of photons in a voxel of maximum intensity was estimated to be 14, using the procedure described by Bornfleth et al. (1998). For each cell nucleus, 16 3D data stacks with a sampling interval of $\Delta t = 20$ min were recorded, resulting in an overall observation time spanning over 4 h. The large time intervals made it possible to analyze the long-term development of nuclear morphology of chromosome territories.

The point spread function (PSF) was determined by recording images of quartz glass microspheres with a fluorescent core (Verhaegh and van Blaaderen, 1994), using the method described by Bornfleth et al. (1998).

Image matching

To correct for the motion of individual cells in subsequent 3D image stacks, a correlation function analysis (CFA) (Jähne, 1993) with four degrees of freedom was implemented. In addition to three translational degrees of freedom, a fourth degree of freedom, the angle of rotation round

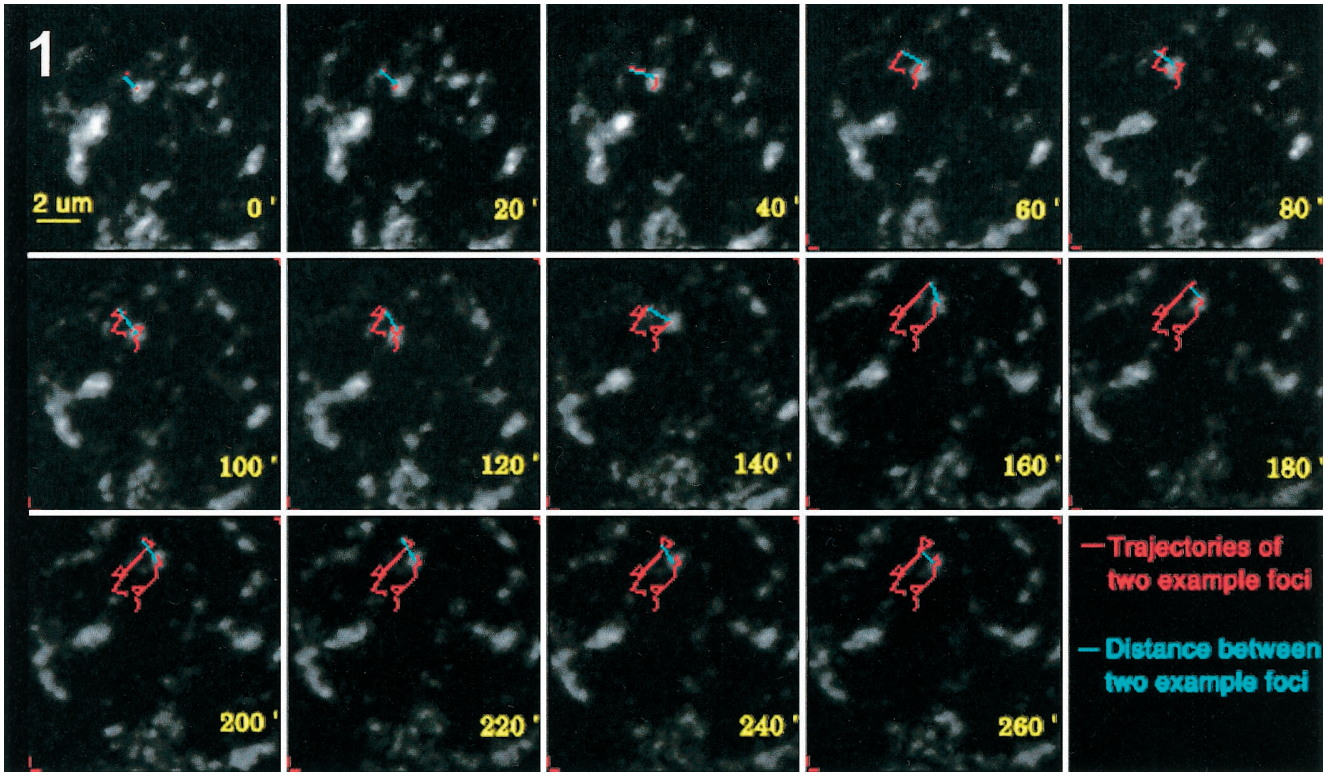

FIGURE 1 Image detail of a neuroblastoma cell nucleus after matching of all subsequent image stacks. Maximum intensity projections at 14 different sampling times are shown. For two example foci, the trajectories (*red*), indicating their individual displacements, and the displacement vectors between them (*cyan*) are shown. Note that these vectors are 2D projections from a 3D data stack.

the optical axis was chosen, because this was the only apparent rotational motion cell nuclei performed in the experiments evaluated.

It was considered sufficient to determine the rotational motion with $\pm 0.5°$ resolution. For a point 58 pixels away from the rotational axis, this corresponded to an error of ± 0.5 pixels. Because the maximum radius of cell nuclei used in the experiments was $\sim$ 7–8 μm, corresponding to 58–67 pixels with the pixel size used, and the rotational axis was near the center of the nucleus, this resolution was sufficient. On average, nuclear radii were determined to be $\sim$5 μm for the almost spherical HeLa cells and between 3 μm (shortest axis) and $\sim$7–8 μm (longest axis) for the neuroblastoma nuclei.

Fig. 2 shows the overlay of two maximum intensity projections of a cell nucleus at different times. Here the rotation angle found was 6°. Over the whole observation period of cells, rotation angles of up to 34° were observed.

Segmentation and tracking of territories and of individual foci

Before any analysis, the time-lapse series of 3D data sets of the recorded cell nuclei were processed with a $3 \times 3 \times 1$ median filter, to reduce the effect of photon noise. To avoid the phototoxic effects of the laser light, the living cells had to be imaged with low laser power. Because the localization accuracy increases with the square root of the number of detected photons (Patwardhan 1997), photon noise is the most prominent source of error in biological experiments with living specimens (Ghosh and Webb, 1994). A background signal due mainly to scattering and autofluorescence was reduced by a global background subtraction. From each voxel of a 3D data set the mean gray value of the respective 3D data set was subtracted. In the following, the labeled chromosome territories or territory subregions were segmented by interactive setting of a global threshold (cf. Gundersen and Jensen, 1987). After segmentation, the features of interest were extracted by a labeling procedure that identified all connected voxels of an object by using the 26-connectivity rule, i.e., all voxels that were connected by a common surface, edge, or, at least, by a common corner. All voxels that were identified as belonging to the same object were used to compute the barycenter, $s = (s_x, s_y, s_z)^T$, of the object (the intensity-weighted analog of the center of mass; Möbius, 1827):

$$s_x = \frac{1}{M}\sum_{i=1}^{N} g_i \cdot x_i, \qquad s_y = \frac{1}{M}\sum_{i=1}^{N} g_i \cdot y_i,$$
$$s_z = \frac{1}{M}\sum_{i=1}^{N} g_i \cdot z_i, \qquad M = \sum_{i=1}^{N} g_i, \tag{1}$$

where g_i is the gray value of the voxel i at the coordinate (x_i, y_i, z_i), and N is the number of voxels belonging to the object of interest.

Fuzzy boundaries of the biological objects made it difficult to define a border between foreground and background voxels. Therefore, and to avoid any bias by interactively choosing a certain gray value threshold, the intensity barycenters were determined for each threshold in a range of reasonable thresholds, which preserved the overall object geometry, and were then averaged.

On a subchromosomal level, the image stacks contained multiple signals of subchromosomal foci with a size comparable to that of the microscopic observation volume (the observation volume is defined as the volume of the PSF at half-maximum; Lindek et al., 1996). They were segmented using a model-based algorithm that detected local maxima and used an iterative region-growing process for the segmentation of individual foci. The basic algorithm is described by Bornfleth et al. (1998). An improved implementation that also models the intensity distribution of individual foci and uses this information to subtract signal from neighbor-

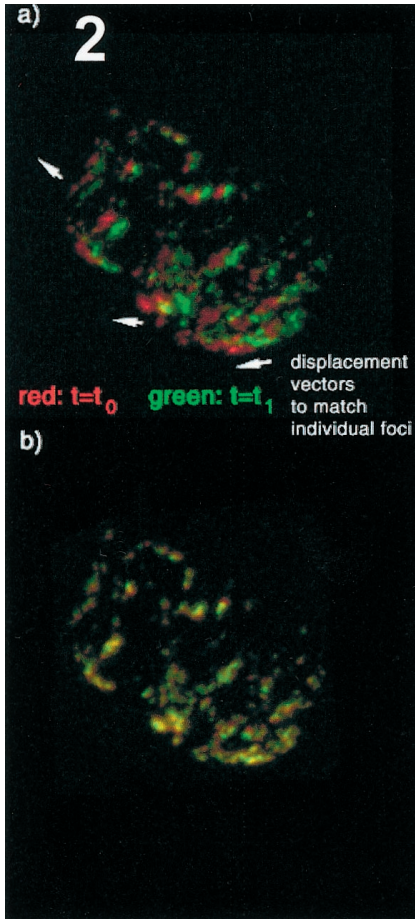

FIGURE 2 Example of the matching of two neuroblastoma cell nuclei by the correlation function analysis. Visual inspection of projection images of the cells at two consecutive times indicated that not only translational but also rotational motion had to be considered (cf. displacement arrows in *a*). In *b*, the projection of the two image stacks after matching with four degrees of freedom (three translational and one rotational) is shown. A rotation of 6° was found.

ing objects is described by Bornfleth et al. (1999). In simulations and experiments, this approach yielded a significant improvement in localization accuracy (Bornfleth et al., 1999). This improved algorithm was used to analyze the present data. Before segmentation of the subchromosomal signals, images were filtered with a $3 \times 3 \times 3$ median kernel, and a global background subtraction was performed.

The analysis of the motion of individual foci required their tracking over subsequent time-lapse image stacks with SPT (Ghosh and Webb, 1994). To improve SPT results, approaches that use features such as size, shape, and intensity, so-called templates, have been developed for 2D (Gelles et al., 1988).

Because DNA foci represent objects with a size comparable to that of the microscopic observation volume, it was difficult to assign stable shape parameters. The template-based tracking algorithm presented here used two templates: the 3D displacement from the object to be tracked to a candidate object, and the difference between the integrated fluorescence intensities (IFIs) of the two objects. The IFI was obtained by multiplying the brightness and the volume found by the segmentation algorithm described by Bornfleth et al. (1998, 1999). This value was a more stable estimate than just the volume or just the brightness. To track an object from one image stack to the next, the maximum allowed displacement of an object, which defined the search volume, was given by the user. The principle is illustrated in Fig. 3. When the template-based tracking was applied in practice, a comparison with manual tracking results showed that an improved performance was obtained by adding the IFI of the spot to be tracked to the maximum difference, i.e., for the spot m at time t_i:

$$\Delta_{\mathrm{IFI,max}}(m, t_i) := \max\{\mathrm{abs}(\mathrm{IFI}(n, t_{i+1}) - \mathrm{IFI}(m, t_i)), n \in [1, \ldots, N]\} + \mathrm{IFI}(m, t_i). \quad (2)$$

This led to an offset on the ordinate in the 2D parameter diagram (cf. Fig. 3). The axes of this diagram were normalized to maximum difference and displacement, respectively (cf. Fig. 3 *d*). Adding the IFI of the spot to be tracked to Δ_{IFI} (cf. Eq. 2) reduced the relative influence of differences in IFI compared to differences in displacement. This reflected the finding that displacement measurements were possible with higher accuracy than IFI measurements with the given photon statistics. An example of application to a real data set is shown in Fig. 4.

Statistical methods for the quantitative analysis of motion

For an arbitrary time interval $\Delta t_j = t_j - t_0 = t_{j+1} - t_1 = \ldots = t_n - t_{n-j}$, the MSD is given by

$$\mathrm{MSD}(\Delta t_j) = \frac{1}{n-j} \sum_{i=j}^{n} [\vec{r}(t_i) - \vec{r}(t_{i-j})]^2. \quad (3)$$

This way of internal averaging over a single particle trajectory implies that, except for Δt_1, the measurements are not independent. According to Qian et al. (1991) the theoretical error (standard deviation) relative to the measured quantity of $\mathrm{MSD}(\Delta t_j)$ is approximately given by

$$\frac{\sigma(\mathrm{MSD}(\Delta t_j))}{\mathrm{MSD}(\Delta t_j)} = \sqrt{\frac{2j}{3(n-j+1)}}. \quad (4)$$

For low numbers of data points in a trajectory, e.g., $n = 14$, which was a value relevant to the measurements presented here, this error can outgrow the value of MSD itself. From a plot of the MSD versus the time interval, three principal types were distinguished within the frame given by Eq. 4, characterized by the equations

$$\mathrm{MSD}(\Delta t) = 6D\Delta t \quad \text{(Landau and Lifschitz, 1966)} \quad \text{(“random Brownian motion”)} \quad (5)$$

$$\mathrm{MSD}(\Delta t) = 6D\Delta t + v^2(\Delta t)^2 \quad \text{(“directed motion”)} \quad (6)$$

and

$$\lim_{\Delta t \to \infty} \mathrm{MSD}(\Delta t) = R^2 \quad \text{(Saxton, 1993)} \quad \text{(“constrained Brownian motion”),} \quad (7)$$

where D is the diffusion coefficient and v is the velocity of directed motion.

With constrained Brownian motion, a large number of measurements are necessary to obtain the radius R that defines the cage size.

The Euclidean distance between two diffusing particles is independent of the matching of subsequent image stacks. If the relative diffusive motion between particles is analyzed, Eq. 3 is modified to evaluate the difference between distances at two sampling times rather than positions:

$$\mathrm{MSD}_{\mathrm{spot2}\to 1}(\Delta t_j) = \frac{1}{n-j} \sum_{i=j}^{n} [d_{\mathrm{spot2}\to 1}(t_i) - d_{\mathrm{spot2}\to 1}(t_{i-j})]^2. \quad (8)$$

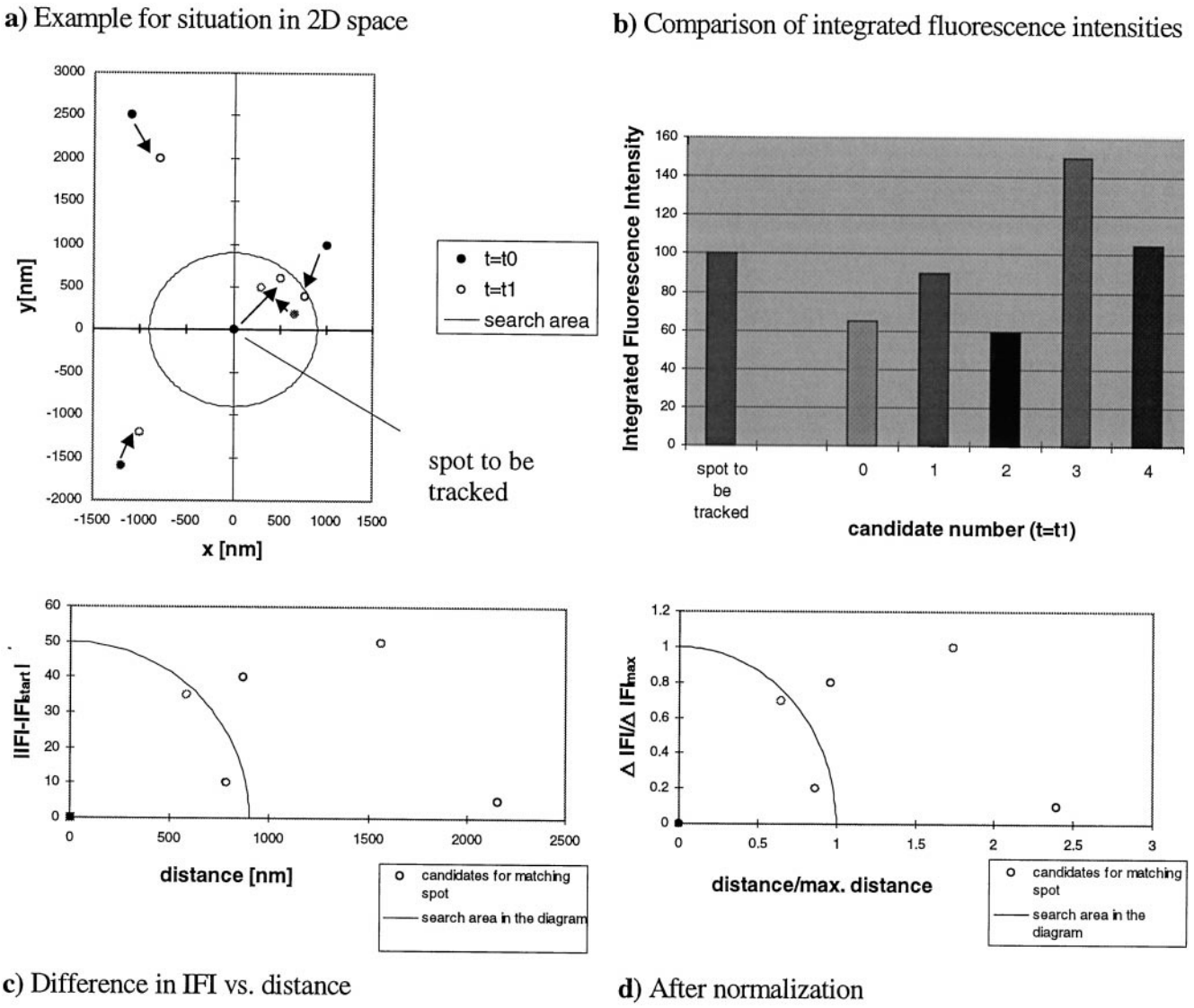

FIGURE 3 Schematic principle of the automated tracking of objects in a time-lapse series of 3D image stacks. For a better illustration of the principle, different objects are denoted by different gray shades. (*a*) In a 2D projection, the search volume for the central object comprises three candidates at the next sampling time, $t = t_1$ (○). The search volume is given by a sphere with a radius of 900 nm. (*b*) For all objects, the integrated fluorescence at $t = t_1$ is compared to the integrated fluorescence intensity (IFI) of the central object at t_0 as a second feature. (*c*) A diagram that shows both features. (*d*) Displacements and the differences in IFI are normalized to the maximum difference (IFI) and to the maximum expected displacement, which corresponds to the radius of the search volume. The object that is closest to the object at the origin is recognized as the matching partner in the next image stack.

It is expected that for two foci that are both subject to random Brownian motion, the diffusion is described by the formula

$$\mathrm{MSD}_{\mathrm{spot2}\rightarrow 1}(\Delta t) = 4D\Delta t \tag{9}$$

(von Smoluchowski, 1917). A transition that occurs during the time of observation (e.g., between free diffusion and directed motion) may not be detected by this type of analysis (Saxton, 1997). Another type of analysis—testing for directed motion between individual observation times—was therefore implemented. If many signals can be distinguished inside a chromosome territory, changes in its conformation can be detected by analyzing the directional movement of the individual subchromosomal foci. Analysis of directional motion has previously been used for the description of the type of cell movement in mounds (Doolittle et al., 1995), where the Rayleigh test (Mardia, 1972) was used to quantify cell motion.

The idea pursued here was to use the movements of subchromosomal foci in chromosome territories to distinguish between "random" and "non-random" conformational changes in the chromosome. The changes were induced by the motion of a few foci or by changes that affected the whole chromosome territory in a similar way. Because the motion inside the territory was of interest, the mean movement of the chromosome territory was corrected for. This was achieved by subtracting the average motion of the foci found from sampling time ($n - 1$) to sampling time (n). The displacement vector $V_i^{(n)}$ that defined the motion of a spot i for a sampling time n was calculated, and the mean motion of the territory was then subtracted:

$$\bar{\vec{V}}^{(n)} = \frac{1}{N_{\mathrm{spots}}} \sum_i (\vec{X}_i^{(n)} - \vec{X}_i^{(n-1)})$$

$$\vec{V}_i^{(n)\prime} = \vec{V}_i^{(n)} - \bar{\vec{V}}^{(n)}, \tag{10}$$

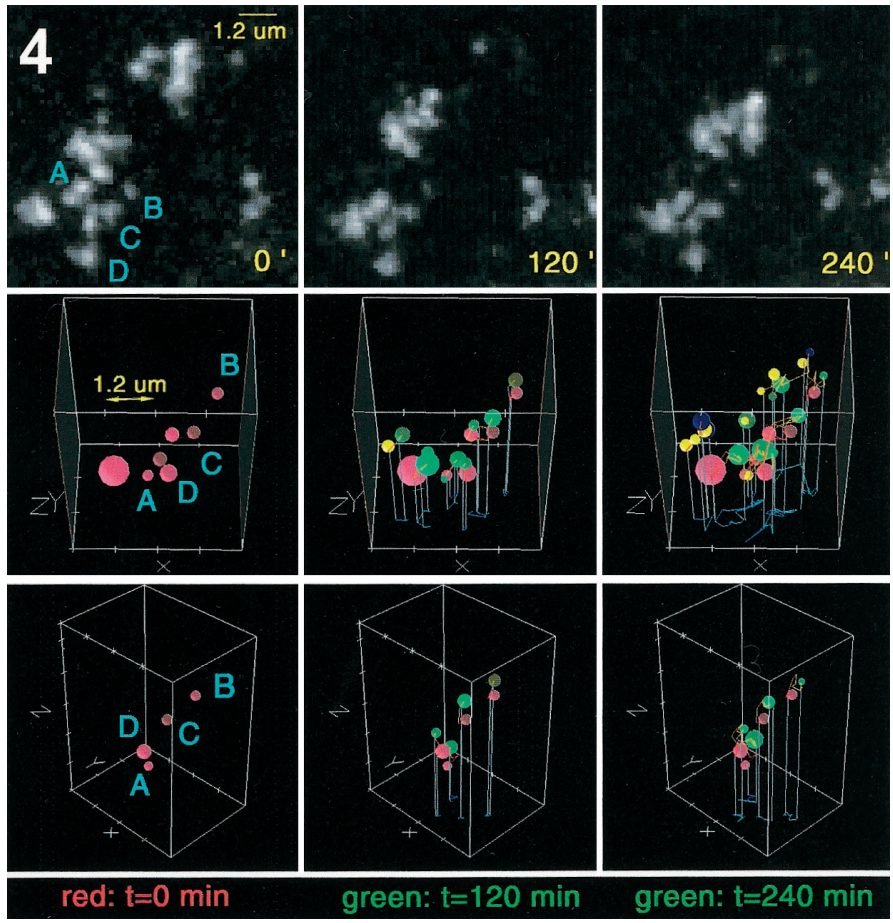

FIGURE 4 Example for the feature-based tracking of objects. *Top row*: Maximum intensity projections of an experimentally observed chromosome territory in a live HeLa cell nucleus at three different sampling times (note that only the area between the points denoted by *A–D* belongs to the territory; the other territory is situated in another image plane and moves away from the example territory). *Middle row*: Four-dimensional image analysis of position and volumes of foci. The foci are shown as spheres with volumes that correspond to the volumes found after segmentation. Red spheres denote the positions and volumes of foci at the starting point of the trajectories at t_0. Yellow spheres denote the foci at a later sampling time ($t > t_0$), e.g., after parting of foci that were merged optically in a previous image stack. Blue spheres denote foci for which no matching foci could be found in the subsequent image stack. Green spheres denote the end points of trajectories. In some cases optical merging of foci led to the merging of trajectories. *Bottom row*: Four foci (*A–D*) that could be tracked in a reciprocally unique way throughout the sampling period.

where $X_i^{(n)}$ denotes the position of spot i at sampling time n.

In Schmidt nets, after Schmidt (1925), the direction cosines of motion projected on the upper or lower hemisphere are plotted. In these equal area projections of the motion directions, the presence of a directed motion of foci in territories and its direction was visualized by the appearance of a clustering around the principal axis. In Fig. 10 *f* a clustering along the optical axis is obvious.

In experimental data sets, an apparent motion is detected, even in fixed targets, because of the inaccuracies of distance measurements. Because of the statistical nature of the errors, the directions of motion that are observed vary arbitrarily. For a fixed target, a random distribution over the hemispheres of the Schmidt nets is expected.

However, the degree of accuracy of distance measurement is greater in the lateral plane (*x-y* direction) than in the axial (*z*) direction (Bornfleth et al., 1998). To prevent artifacts induced by these differences, it was necessary to correct the measured displacements on the grounds of positioning inaccuracy. The heuristic approach,

$$x' = x\frac{1}{\sqrt{1+\left(\frac{\sigma_x}{x}\right)^2}}, \qquad y' = y\frac{1}{\sqrt{1+\left(\frac{\sigma_y}{y}\right)^2}},$$
$$z' = z\frac{1}{\sqrt{1+\left(\frac{\sigma_z}{z}\right)^2}}, \tag{11}$$

where σ_x, σ_y, and σ_z = errors (standard deviation) of distance measurement in the *x*, *y*, and *z* directions, respectively, gave the desired result.

To decide whether an observed motion inside chromosome territories was "random" or "directed," a statistical analysis of the directions according to the method of Bingham (1964) was performed (see Appendix). The method yielded an estimator S_u that was expected to be distributed according to the χ^2_5 distribution under the hypothesis of uniformity.

Simulation of time-lapse confocal imaging of subchromosomal targets

To discriminate between biologically relevant movements and artifacts introduced by the imaging process and the image evaluation procedure, it was necessary to test the algorithms described above for their specific performance. Therefore, the behavior of fluorescence-labeled cell nuclei in vivo was simulated by virtual microscopic imaging following a model distribution of targets. Model territories consisted of 25 spherical targets (250-nm radius) distributed randomly in a spherical volume representing the territory (radii 1.92 μm × 1.92 μm × 1.92 μm). Targets were allowed to touch, but not to overlap. Images were created by convolution of the data sets with the measured Cy3-PSF (voxel size 120 nm × 120 nm × 440 nm). Subsequently, noise was added. Uniform background noise was simulated by a Gaussian distribution of gray values (σ = 12 gray values, mean gray value = 20). Photon shot noise was simulated by a Poisson process applied to the convoluted simulation image. A voxel of maximum intensity (200 gray values) corresponded to 14 detected photons, resulting in an SNR of ~3.7 (Bornfleth et al., 1998). The final simulation image was obtained by adding the uniform background image and the convoluted image.

Time-lapse imaging was simulated in two different ways:

Type A: Targets did not move between "observation times." These simulations were used to find the apparent motion, which was simply due to noisy imaging conditions.

Type B: Targets moved randomly between "observation times." The motion was defined by a random displacement $d = \sqrt{d_x^2 + d_y^2 + d_z^2}$, with

an absolute value chosen randomly from the interval [0, . . . , 285 nm] for each of the Cartesian coordinates:

$$d_x \in [0 \ldots 285\ \text{nm}/\sqrt{3}], \qquad d_y \in [0 \ldots 285\ \text{nm}/\sqrt{3}],$$

$$d_z \in [0 \ldots 285\ \text{nm}/\sqrt{3}]$$

and mutual volume exclusion.

This type of simulation was used to test the accuracy of measurement of diffusion coefficients and to test the performance of the statistical test for directed motion.

For type A simulations, 12 "observation times" were recorded. For type B simulations, 16 sampling times were chosen. In the experiments, 12–14 sampling times could be evaluated for a typical DNA focus. Some data points were lost because foci occasionally left the field of view.

Measurement of diffusion coefficients of test objects

To test the confocal microscopic imaging system and the image-processing algorithms as a whole, diffusion coefficients of test objects in a medium of known viscosity were experimentally determined. The expected diffusion coefficient for spherical objects was given by

$$D = \frac{kT}{6\pi\eta r} \tag{12}$$

where η denotes the viscosity and r is the radius of the objects.

Fluorescent latex microspheres (Tetraspek, $r = 280$ nm; Molecular Probes) were used as test objects. The radius was chosen to be close to the experimentally determined mean radius of foci in territories ($r = 250$ nm; see Results). The embedding medium used was Zeiss 1.514 N immersion oil (with a viscosity of $\eta = 6.84\text{E-}3$ kg/(s cm) for $T = 293$ K).

A total number of eight time-lapse series of 3D data sets were acquired with a Leica TCS NT confocal laser-scanning microscope. At 10 sampling times with intervals of 12 s, 3D data sets of microspheres were acquired (voxel size 155 nm × 155 nm × 608 nm).

To match the consecutive 3D data sets, stationary beads that had been dried on the cover glass were used. For tracking of the individual beads the image analysis algorithms described above were used.

RESULTS

Analysis of apparent motions in simulated data sets

Even in the case of stationary targets, a small apparent motion of their intensity gravity centers was observed because of the imaging conditions and the image evaluation procedure. If many signals with overlapping diffraction patterns were present, systematic localization errors were added to the inaccuracies caused by photon shot noise and image matching.

For a better discrimination between such apparent motions and real motions, simulated static images were created to closely model the experimental conditions present in replication labeling experiments, where many signals were present in a chromosome territory. The simulations showed that the radii of foci were recovered after segmentation with high accuracy (Fig. 5 *c*; cf. also Bornfleth et al., 1998). For comparison, the fluctuations of experimentally found radii of foci are presented in Fig. 5, *a* and *b*. These in vivo measurements revealed mean radii of foci of 250 nm in both neuroblastoma and HeLa cell nuclei.

SPTs were used for the calculation of diffusion coefficients if the target trajectory could be tracked in a reciprocally unique way throughout the entire recording time (i.e., if no optical merging or parting of targets was observed; for an experimental example see Fig. 4). Fig. 6 *a* shows a typical plot of mean squared displacement versus time (MSD-*t* graph) for three simulated stationary foci in (type A) simulations. Fig. 6, *b* and *c*, shows typical MSD-*t* graphs for the type B simulation with small random displacements before and after virtual microscopic imaging.

Accuracy of diffusion coefficient measurement and of statistical analysis of directed motion in simulated data sets and in experimental bead measurements

The diffusion coefficient D was calculated from the SPTs of simulated foci. Fig. 7 *a* shows the apparent diffusion coefficients that emerged for type A (stationary) and type B (random displacement) simulations versus the true values of D. Even if no motion was present, a mean value of $D = 2.3 \times 10^{-14}$ cm^2/s was obtained. For the type B simulation, the value of D found after imaging was approximately twice as high as the true value (7.2×10^{-14} cm^2/s versus 3.8×10^{-14} cm^2/s). However, the correct order of magnitude was obtained. Fig. 6 indicates that for stationary targets (type A simulation), an apparent "constrained diffusion" was observed. This was not the case for the type B simulation, where a "free diffusion" was observed within the time range studied, consistent with the true behavior.

In experimental SPT measurements of diffusing microspheres embedded in immersion oil, a similar result was found. SPTs of microspheres were only used for the computation of diffusion coefficients if the microspheres could be tracked throughout the entire observation time. This resulted in a total number of entirely tracked microspheres of $N = 27$. Diffusion coefficients were calculated as described in Eq. 6. The expected value of $D = 1.13 \times 10^{-11}$ cm^2/s (cf. Eq. 12) was exceeded, but measured values were on the same order of magnitude as the expected value (see Fig. 7 *b*).

The type B simulation was used to test the statistical approach for directional motion analysis. Because the 25 "foci" in the test "territory" were moved independently (small random displacements), with the only constraint that overlap was prohibited, a low test value S_u was expected. Fig. 7 *c*) shows that this was indeed the case. Fig. 7 *c* also gives the test values S_u obtained after the imaging process, which also lie below the 5% significance level.

Diffusion-like movements of territories and subchromosomal foci in experimentally obtained images of cell nuclei

In the replication-labeling approach described here, a multitude of signals distributed over several labeled territories in a given cell nucleus were obtained experimentally.

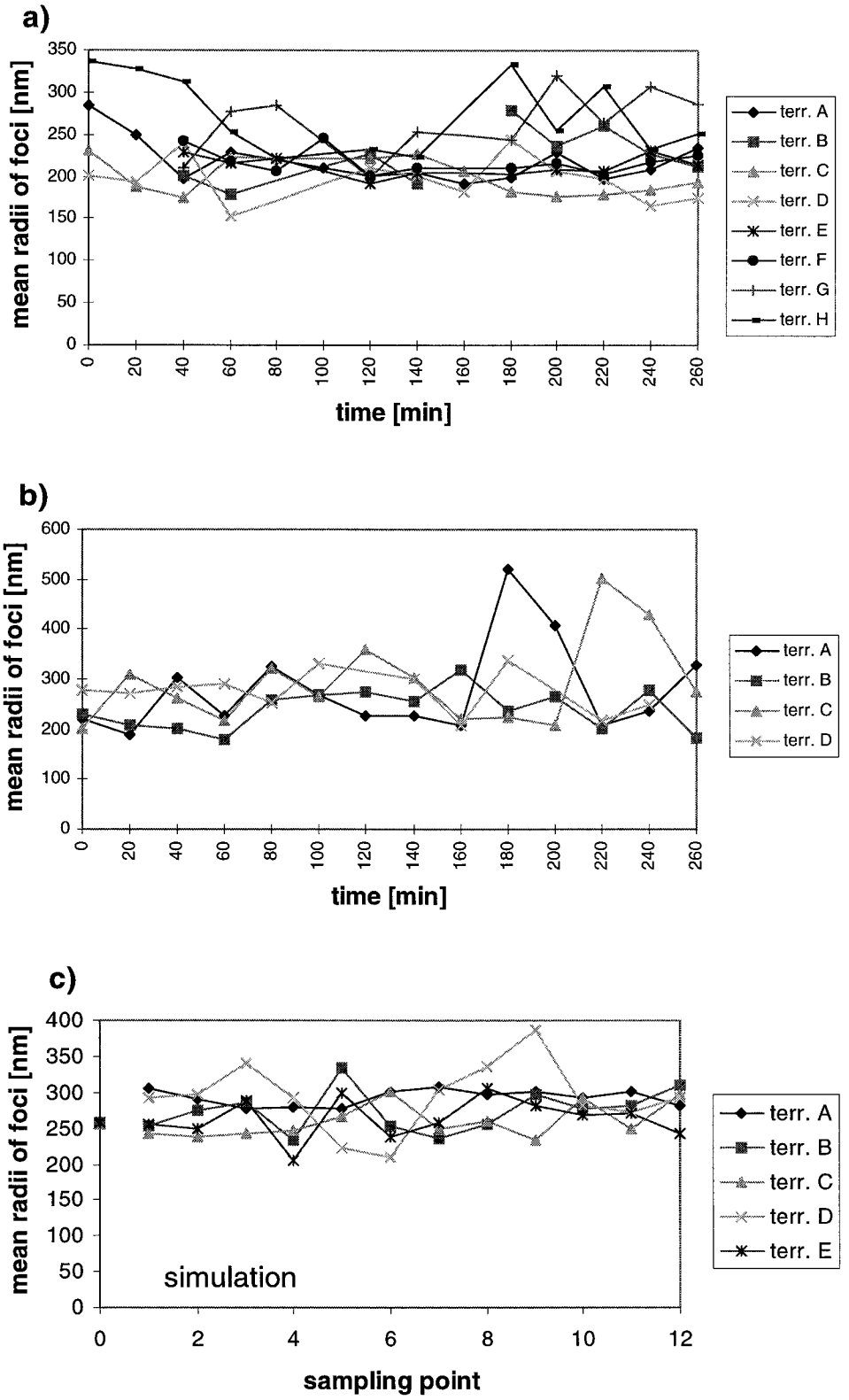

FIGURE 5 Time variation of apparent mean radii of foci experimentally found in HeLa cell nuclei (*a*) and in a neuroblastoma cell nucleus (*b*). Most apparent radii are in a range between 200 nm and 350 nm. The "outliers" in *b* are caused by territories with very few foci, where two foci merged optically. (*c*) For comparison, the variation of apparent mean radii as a function of "observation time" was determined by simulation of stationary model "territories." Here all model radii were assumed to have a "true" diameter of 250 nm (denoted as a *square on the ordinate axis*). The simulation shows that the radii found by the algorithm were close to the true values but were often somewhat higher because of optical merging of neighboring foci.

All detectable fluorochromes were incorporated into the nuclear DNA so that the preparations were virtually free of background and all signal observed corresponded to labeled DNA. This was due to several factors. First, fluorochrome-labeled nucleotides rapidly leave the nucleus after microinjection into the nucleus and are stably packaged into cytoplasmic vesicles. Thus, a few hours after microinjection, almost no free labeled nucleotides were available within nuclei and whole cells (Fauth, 1998). In addition, the few free nucleotides that might have been present were diluted

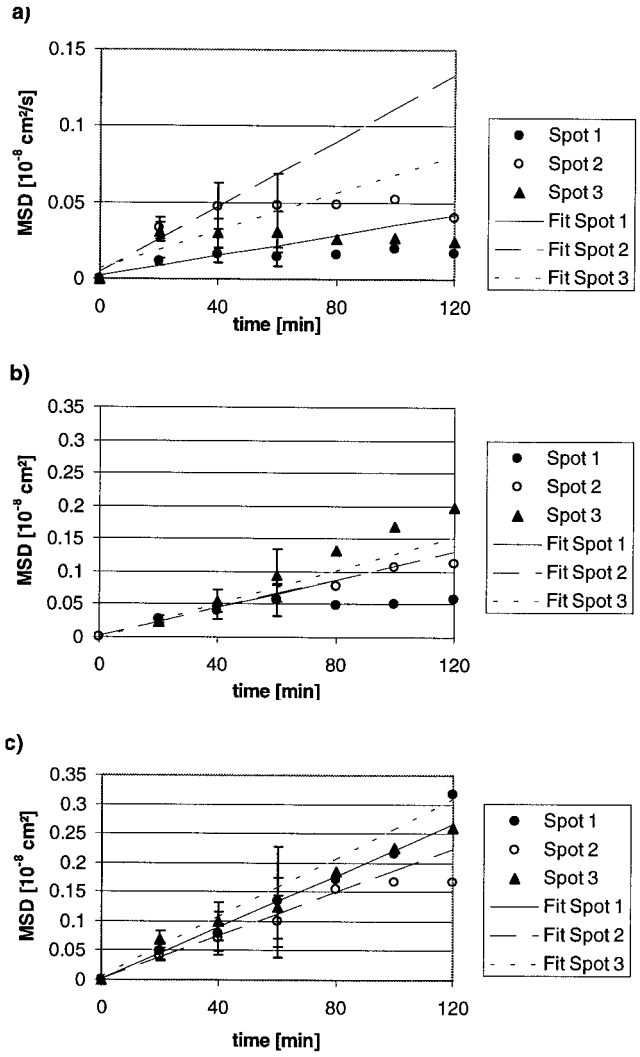

FIGURE 6 Mean square displacements (MSDs) of single foci tracked in simulated model chromosome territories. (*a*) For stationary foci (type A simulation), an apparent motion was detected because of noise and optical merging of closely neighbored foci in some of the image stacks. All foci performed an apparent "constrained diffusive" motion. The errors of the data points used for least-squares fitting are also indicated. For clarity, only three foci are displayed in the plot. (*b*) Type B simulation (assumed small random displacements of foci) resulted in a "free diffusion" of foci, within the range of "observation times" studied. (*c*) After virtual microscopy and 3D image analysis, the apparent diffusion is more strongly pronounced than originally assumed in *b*.

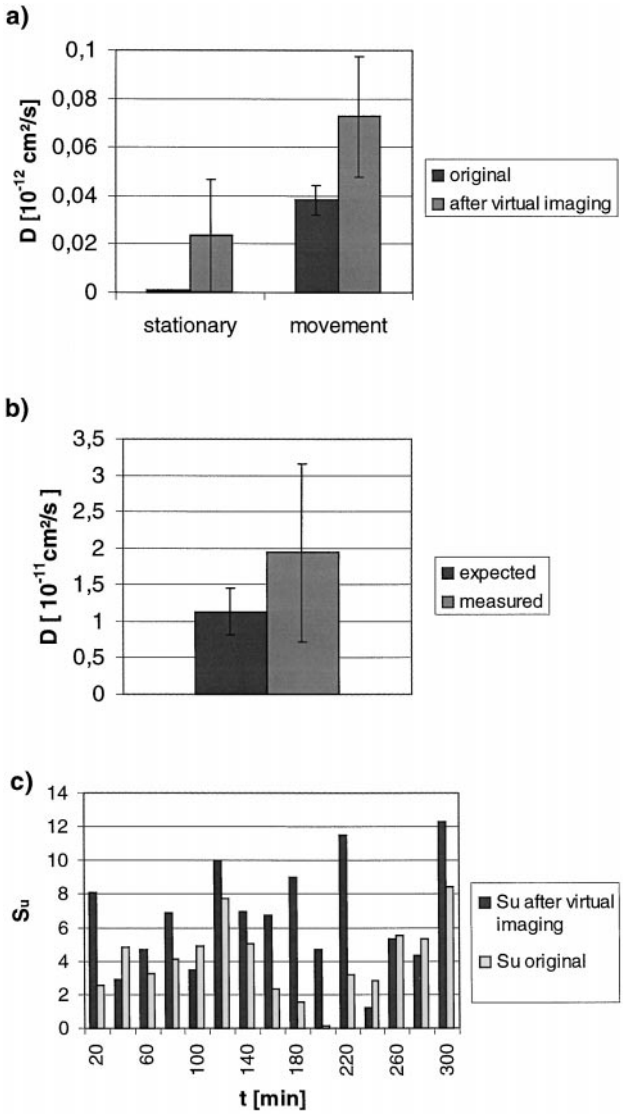

FIGURE 7 (*a*) Mean diffusion coefficients found in type A simulations (stationary model foci, *left*) and type B simulations ("free diffusive motion" of foci, *right*). Because of noise and optical merging and parting of foci, a "diffusion coefficient" that is shifted toward higher values was obtained after the virtual imaging process and image analysis. Nevertheless, the "diffusion coefficients" found for "diffusing foci" were on the correct order of magnitude. Error bars denote the standard deviation. (*b*) Mean "diffusion coefficients" found in experimental time-lapse series of 3D data stacks with microspheres (radius 280 nm). Because of the limited localization accuracy, a higher mean value than expected was measured ($(1.94 \pm 1.22) \times 10^{-11}$ cm^2/s versus $(1.13 \pm 0.32) \times 10^{-11}$ cm^2/s). The correct order of magnitude, however, was obtained. (*c*) Test value S_u for "directional motion" assumed to be in a simulated chromosome territory (type B simulation) at 16 different sampling times. The motion of foci inside the model territory was assumed to be random. This resulted in a low value of S_u for the original displacement data (*light shaded columns*). After virtual microscopy and image analysis, most values for S_u were raised compared to the true values. However, the 1% confidence threshold of the test statistics χ^2_5 was not exceeded.

during cell divisions. All cells imaged went through at least two mitoses after cell division, as the segregation of labeled and unlabeled chromosomes indicates. Time-lapse series of mitotic labeled cells clearly demonstrated that all fluorescence was confined to chromosomal DNA (Fauth, 1998) (cf. also Manders et al., 1999).

For the analyses of the experimental data presented here, only foci that could be clearly assigned to a territory because of the joint motion with other foci were evaluated. Thus in some cases, subterritories rather than whole territories were analyzed. For simplicity, the term "territory" is used here to describe either territories or subterritories.

On the whole, experimental 4D data of 13 territories in five cells were analyzed over sequences comprising 14 sampling times. Altogether more than 1100 foci were seg-

mented and analyzed. At the first sampling time, a total of 110 foci were segmented in these territories, corresponding to a mean number of 8.5 foci found in a territory. Of the 110 foci, 31 could be tracked throughout the time-lapse series. For directional motion analysis, a much higher percentage of foci could be used because tracking through the whole series was not required.

The matching of subsequent image stacks implied the subtraction of the net movement of the cell nucleus. The remaining motion was due to the movement of whole chromosomes in the cell nucleus and to the movement of subchromosomal foci within the territories. Changes in the shape of the nucleus due to external forces, induced by the cytoskeleton, for example, may also have played a role. The way in which changes in the nuclear shape affect chromosomal motion depends on the nuclear architecture. Because nuclear architecture is still a topic of major discussion, no correction was performed for a possible motion of chromosomes due to external forces.

Fig. 8 shows the experimentally measured 3D distances between the barycenters of individual chromosome territories in three different nuclei. The graphs show that individual nuclei displayed a different type of behavior: relative changes in distance between territories were in the range of 0–2.5 μm within the observation period.

Fig. 9 *a* shows the experimentally determined "diffusion coefficients" for individual foci and territory barycenters that were obtained from MSDs by weighted parameter fitting of the first four data points (up to 60 min). No attempt was made in this case to obtain a lower limit for the biologically meaningful diffusion coefficient by simulation; the reason for this was the lack of a reliable simulation of the rotational movements of cells. The data show a marked difference between neuroblastoma cell nuclei (*left*) and HeLa cell nuclei (*right*). The motion of individual foci was assigned to one of three types ("free diffusion," "directed motion," or "constrained diffusion"; cf. Eqs. 5–7), according to the progress of mean square displacement from data points 4 to 7 (80 min to 140 min). Within these time limits, in neuroblastoma nuclei, 10 of the 13 foci appeared to carry out a "free diffusion." For three foci, the motion was assigned to the "directed motion" category. In the neuroblastoma nucleus diffusion coefficients of whole territories (time intervals up to 60 min evaluated) were smaller than those for individual foci. In HeLa cell nuclei, the measured "diffusion coefficients" were already close to the detection limit.

This classification gave only a rough estimate, because the individual errors of measurement were high. For HeLa nuclei, "free diffusion" was observed in 11 cases, "directed motion" was observed in five cases, and "constrained diffusion" was observed in one case. In simulated stationary territories, "constrained diffusion" was observed in 13 cases, and "free diffusion" was observed in four cases. This means that although "diffusion coefficients" observed in HeLa nuclei were occasionally as low as the highest ones found for stationary simulated chromosome territories, the MSDs showed a different behavior. Because in the experiments reported here, interobservation intervals were higher than the overall observation times in a previous experiment (Marshall et al., 1997), the "constrained diffusion" type found in those experiments may be superimposed on the long-time-scale motions measured in this report.

In the case of an independent motion of targets in a cell nucleus, the analysis of the diffusion between two targets ("mutual diffusion") was expected to yield the same result within the statistical error margins as taking the sum of their individual diffusion coefficients, when motion was projected onto their connecting line.

The distribution of "mutual diffusion coefficients" between subchromosomal foci in a territory measured in neuroblastoma and in HeLa nuclei is shown in Fig. 9 *b*. They are smaller than the individual "diffusion coefficients" of foci (Fig. 9 *a*) by approximately one order of magnitude. This indicates that foci in a territory do not move independently. However, the higher degree of motion of individual foci could also be due to a correlated movement of larger parts of the nucleus, due to external forces, for example. To evaluate the influence of this type of movement, the distances between foci located in different chromosome territories were analyzed. To obtain information about "mutual diffusion" between foci located on different territories, pairs of foci with similar individual diffusion coefficients were matched up. Fig. 9 *c* shows that "mutual diffusion coefficients" inside territories are significantly smaller than "mutual diffusion coefficients" between foci in different territories. These again are smaller than the mean of the "diffusion coefficients" for individual foci.

Two factors can be responsible for the differences:

1. Correlated motion of larger parts of the nucleus due to external forces.

2. Apparent motion due to imperfect matching of the nuclei in subsequent image stacks. Although the correlation function analysis gave well-defined maxima, the matching did not attain subvoxel accuracy. Some of the observed displacement of individual foci was due to this subvoxel error. The measurement of distances between different foci in the same nucleus was not affected by the error.

Visual inspection of the motion of foci in the nuclei over time suggested that both effects played a role. Despite these effects, the "mutual diffusion coefficients" between foci of different territories were still significantly higher than the "diffusion coefficients" between foci within the same territories.

Directional motion within chromosome territories

In territories where many foci could be distinguished, a different approach to the statistical analysis of motion was possible. Instead of averaging the motion of a single subchromosomal focus over the whole period, all displacement vectors of foci in a territory were used to test for the

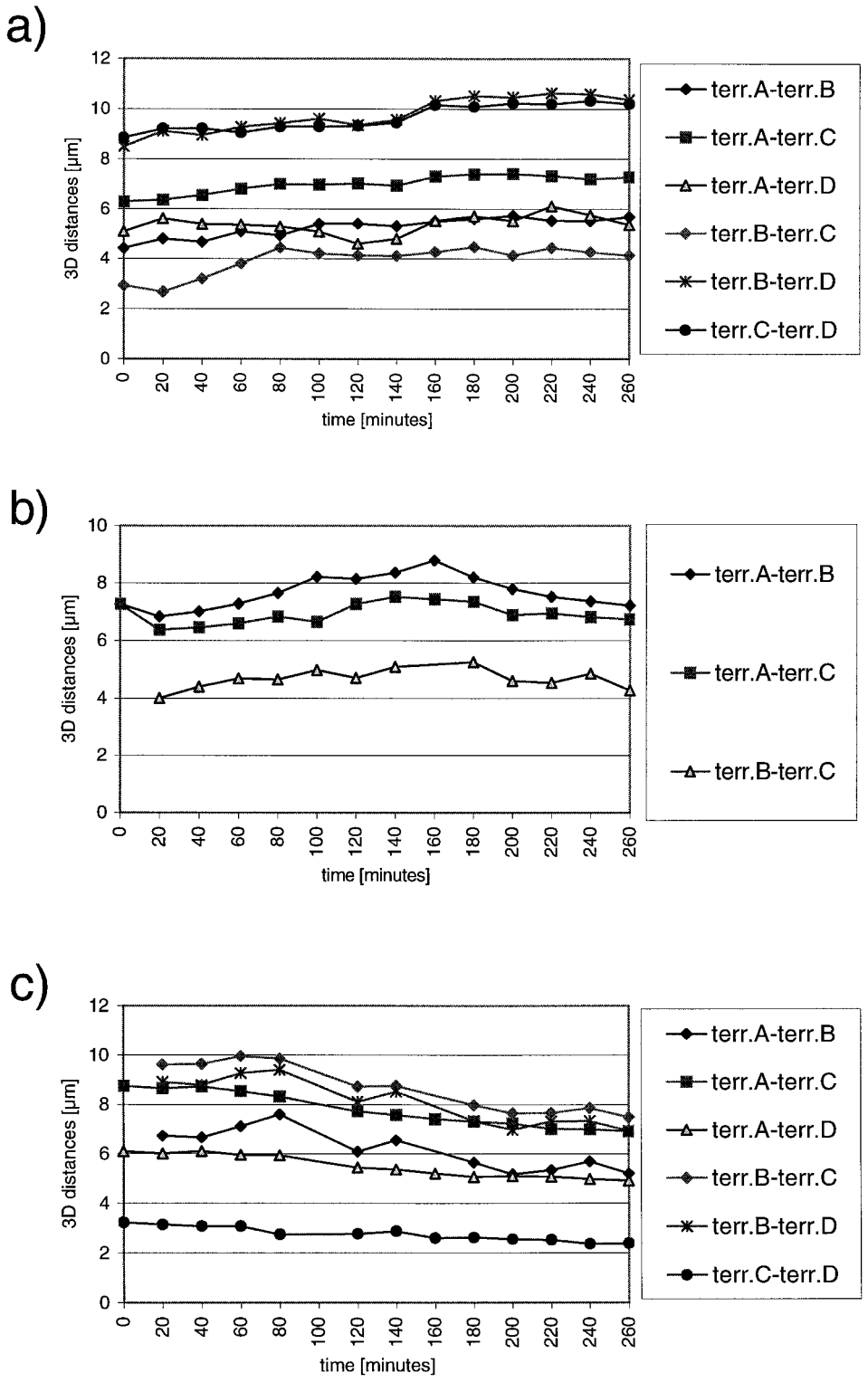

FIGURE 8 Three-dimensional distances experimentally measured between the intensity barycenters of chromosome territories in a neuroblastoma cell nucleus (*a*) and two different HeLa cell nuclei (*b*, *c*). Intracellular distances between territories underwent changes of up to 2.5 μm during the observation period. The nucleus depicted in *b* suggests an oscillatory behavior.

uniformity of motion between only two sampling times. In this way, a possible transition from "random" to "directed" motion could be detected. Foci were tracked from one sampling time to the next. This yielded higher numbers of foci that could be matched with a uniquely defined partner compared to the MSD approach, which required tracking over the whole observation period. For the correction of displacements according to Eq. 11, the values $\sigma_x = \sigma_y = 23$ nm and $\sigma_z = 70$ nm were assumed (cf. the results for low photon statistics quoted by Bornfleth et al. (1998)). The high value for the *z* direction is due to the large voxel size in axial direction. Fig. 10 shows the experimental test values

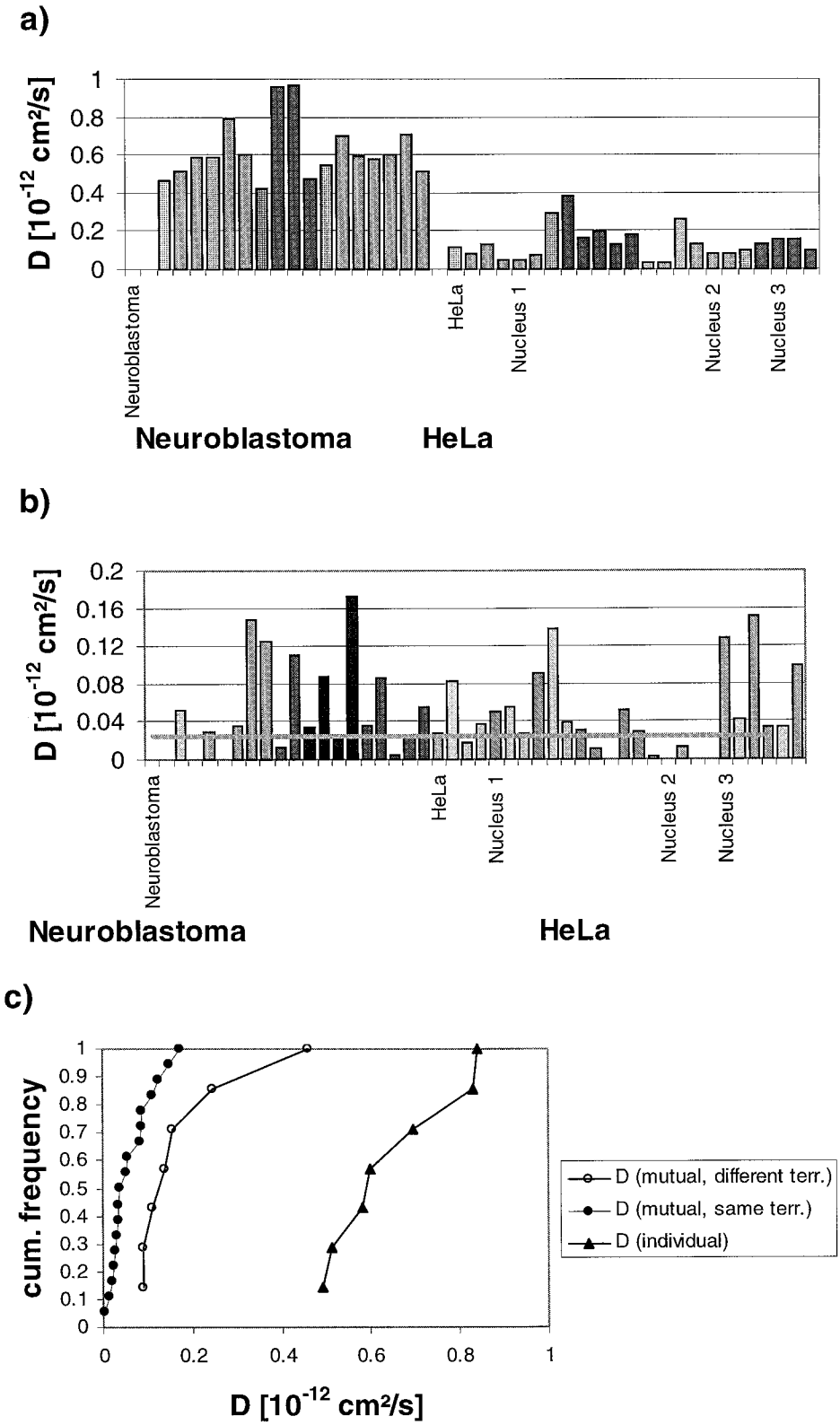

FIGURE 9 Experimentally obtained "diffusion coefficients" *D* measured for chromosome territories and for subchromosomal foci. (*a*) Individual *D* values obtained after image matching. For each territory, the *D* value of the whole territory is given as the leftmost column (*grid hatching*). The *D* values of foci located within that territory are depicted to its right. (*b*) *D* values obtained by analyzing the relative motion between foci ("mutual diffusion") located within the same territory. The absolute values observed were smaller than those obtained for individual foci by one order of magnitude. For comparison with the results of simulation, the horizontal line denotes the mean value obtained for stationary targets (type A simulation). It can be regarded as a detection limit for the experimental setup used. (*c*) Cumulative frequency of *D* values in a neuroblastoma cell nucleus obtained for individual foci, "mutual diffusion" between foci in the same territory, and "mutual diffusion" between foci located on different territories that had similar individual *D* values.

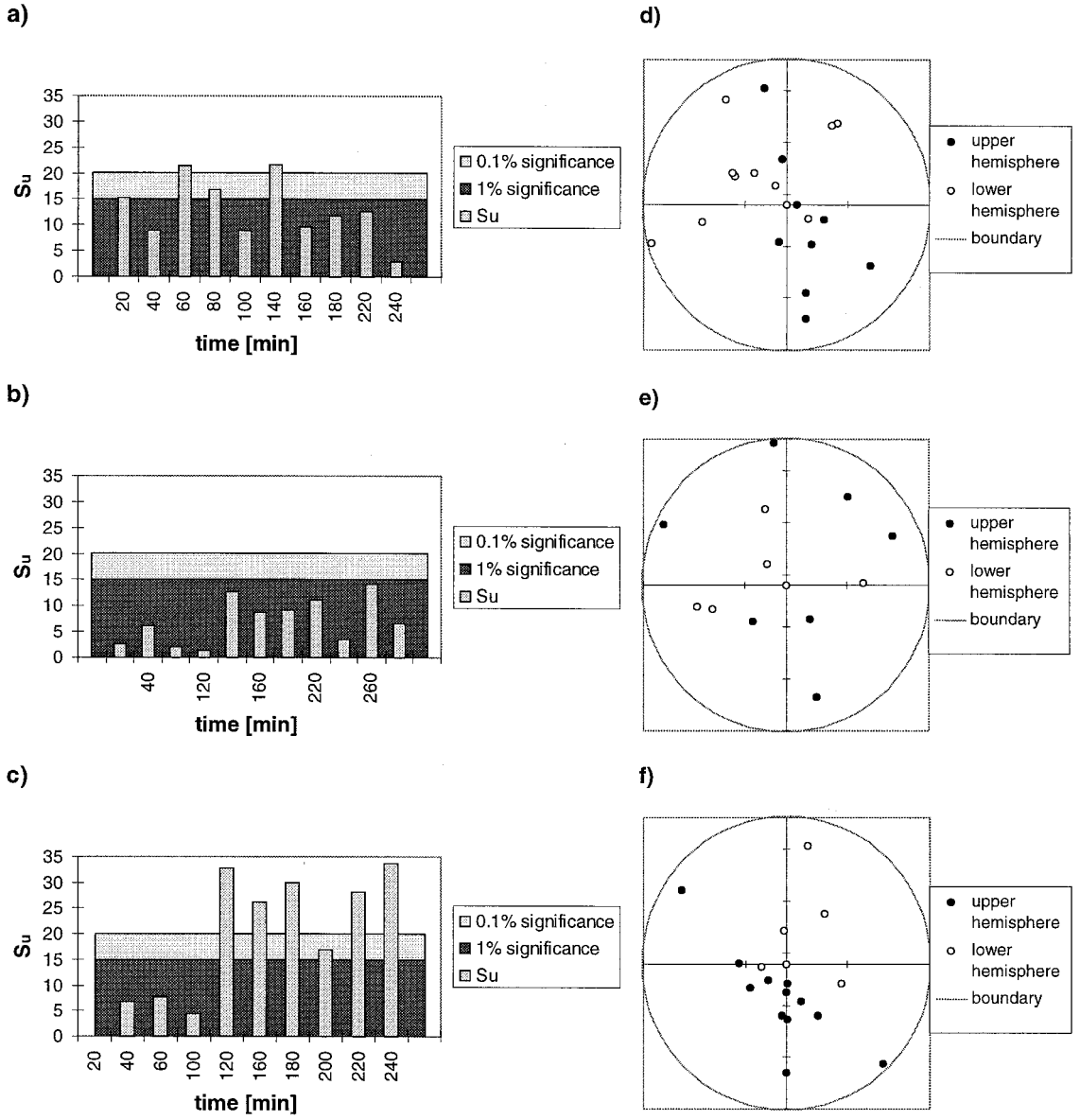

FIGURE 10 "Directional motion" analysis of experimental observation of subchromosomal foci within chromosome territories in live cells. (*a*) In a neuroblastoma territory (territory *D* in Fig. 8 *a*), the 0.1% confidence threshold for the test statistics was exceeded at two different sampling times. (*b*) In an example HeLa territory (territory A in Fig. 8 *b*), no "directional motion" was observed during the observation period. (*c*) In a second HeLa territory (territory A in Fig. 8 *c*), directional motion was frequently observed. (*d–f*) Equal area projections (Schmidt nets) of the motion directions of foci for one example sampling time for each of the territories (sampling time at 80 min with 19 tracked foci, 240 min with 12 tracked foci, 120 min with 16 tracked foci). The poles of the hemispheres are defined by the direction of the optical axis. In *d* and *f*, the clustering of directions around a predominant axis is obvious.

S_u found for three different territories. The 0.1% confidence threshold is exceeded twice for the neuroblastoma territory in Fig. 10 *a*. It is crossed frequently for the HeLa territory depicted in Fig. 10 *c*, whereas it is not exceeded for the other HeLa territory (Fig. 10 *b*) (cf. the results for "random motion" in Fig. 7 *c*). As an example, Fig. 10, *d–f*, shows Schmidt nets of the territories analyzed at three sampling times. It is evident that a clustering of the displacement angles in certain areas occurs in Fig. 10, *d* and *f*, whereas no clustering is observed in Fig. 10 *e*.

DISCUSSION

In this report, an approach is described for the quantitative 4D (3D + time) analysis of the dynamics of nuclear structure in living human cell nuclei.

The experimental approach to such a 4D analysis differs from earlier approaches: because of a recently developed labeling technique (Zink and Cremer 1998), it became possible to analyze many distinct signals simultaneously within the same live cell nucleus. This made it possible not only to analyze the "diffusive motion" of a single small fluorescent

target, but also to compare "diffusion coefficients" within chromosome territories with those obtained for "mutual diffusion" between foci located in different chromosome territories. Furthermore, the presence of 10–25 signals inside a chromosome territory for the first time gave sufficient information to allow "directional motion" measurements in territories of living cells between just two sampling times by applying suitable statistical tests. The two different types of motion analysis combined an analysis over a long observation period (~4 h) with an analysis of motion at short time scales (~20 min), using the same type of data.

Because of possible phototoxic effects, the intensity of excitation light has to be kept at a very low level, implying weak fluorescence signals. This constraint can lead to erroneous results when the centers of gravity of small labeled targets are computed. To evaluate the influence of the imaging conditions present in these 4D confocal space-time images on the statistical data analysis, two types of simulation ("stationary" and "randomly diffusing" targets) were performed. The number and size of the targets, as well as the photon statistics, were estimated from images of living cells (cf. Zink et al., 1998a). This ensured that the simulations gave an estimate that was relevant to the biological experiments. In both types of simulation, the "diffusion coefficients" obtained by SPT and a weighted fit to the MSD of individual targets (cf. Saxton 1997) were higher than the true "diffusion coefficients." This result was expected because the localization error adds to the "true" diffusion coefficient. However, the calculated results had the correct order of magnitude. A similar result was obtained when diffusion coefficients of beads embedded in immersion oil of known viscosity were measured. These results imply that great care has to be taken when analysis methods based on the localization of weak fluorescent targets are used. Depending on the amount of true motion of the targets, photon shot noise as well as a possible optical merging or mistracking of targets can have a major influence on the results of SPT analyses: a high degree of motion reduces the relative influence of photon shot noise, but increases the probability of optical merging or mistracking.

Type B simulations (assuming small random displacements between observation times) were also used to evaluate the newly implemented algorithm for the detection of directional motion of foci within their territory. This algorithm used the angles rather than the absolute value of the displacement vector of a focus. When type B simulations were used, the 1% confidence threshold of the χ_5^2 test was not exceeded.

The analysis procedures were applied to the 4D analysis of experimentally obtained confocal 3D images of human cell nuclei, which displayed a number of replication-labeled chromosome territories. In general, two constraints limit the motion of chromosome territories and their constituents: the nuclear envelope, which serves as a constraint for the motion of both whole chromosome territories and subchromosomal foci, and the chromosome territories themselves limiting the motion of their subchromosomal entities. The way in which the nuclear and chromosomal architectures limit the motion of subchromosomal foci is currently under extensive discussion (Marshall et al., 1997; Berezney et al., 1995; Cremer et al., 1995, 1996; Zink and Cremer, 1998; Yokota et al., 1995).

The "diffusive" motion of individual subchromosomal foci, as well as of whole territories, was analyzed by SPT. Here the accuracy was limited not only by the factors mentioned above, but also by the image matching that preceded further analysis. In the time range observed, the results were compatible with a "free diffusion" of subchromosomal foci with small diffusion coefficients ($\sim 0.5 \times 10^{-12}$ cm^2/s in a neuroblastoma cell nucleus). The matching step could be avoided when the relative motion of foci located on different territories is computed, as described by Marshall et al. (1997). "Diffusion coefficients" of such individual foci obtained in the neuroblastoma cell nucleus were lower ($\sim 0.15 \times 10^{-12}$ cm^2/s), but they were still higher than those found between foci located within the same territories ($\sim 0.05 \times 10^{-12}$ cm^2/s). Comparing the results of "mutual diffusion" analysis, it can be concluded that a reduction in mutual motion takes place within chromosome territories. In the range observed, these results differ from earlier reports that diffusion is constrained to a very small radius within the nucleus (Marshall et al., 1998). However, the nuclei studied here were of a largely different type (human tumor cells versus *Drosophila melanogaster* cells); in addition, widely different observation periods were used. Our observations, which were made at much larger time scales, suggest a compartmentalized motility in the nucleus, consistent with present models of nuclear architecture (Cremer et al., 1993, 1996; Lamond and Earnshaw, 1998). The three levels of motion that we observed hint toward a complex architecture within the cell nucleus, capable of setting up constraints and allowing correlated motions of elements within a part of the nucleus. This type of motion might be induced by the cytoskeleton, organizing the 3D shape of the cell nucleus in a tensegrity-type fashion (Ingber, 1993). In future experiments, it will be important to analyze quantitatively the influence of the cytoskeleton on such motions inside the nucleus.

When we look at the test for "directional motion" within territories, the results indicate that occasionally "directional motion" does take place within some territories. A preferential axis of motion of subchromosomal foci was frequently found in one of the three investigated territories. In a second one, the 0.1% confidence threshold was exceeded at two sampling times. The third territory did not show a directional change of conformation. These first results indicate that both "random motion" and "directional motion" are present in human cell nuclei. Again, an induction of chromosomal motion by extranuclear forces is possible, as suggested by Maniotis et al. (1997).

So far, the results obtained from different studies investigating chromatin motions in eukaryotes did not indicate that motor proteins are really necessary to drive chromatin movements (with the exception of nuclear rotation) (see Zink and Cremer, 1998, and citations therein). The velocity of all movements observed so far is in the range of "diffusional" movements. However, this does not mean that slow motor protein-driven movements are not involved. In particular, the "directed" motions are candidates for motor protein-driven movements, although the velocity is in the range of "diffusional" motions. An answer to this question will only be obtained by more elaborate biological experiments involving the poisoning of motor proteins. Another unresolved question is whether tethering and specific release to underlying substructures (e.g., nuclear lamina) are involved in the regulation of chromatin dynamics. This question can also be addressed by the use of specific drugs, as already done by Marshall et al. (1997).

To unravel the different types of chromatin motion within cell nuclei, it will be indispensable to better understand fundamental biological processes, like replication and transcription, which all require small-scale motion. So far, these processes are well understood on the molecular level. A variety of studies indicate that they are also well organized spatially within the nucleus. However, the dynamics of the highly controlled spatiotemporal patterns of replicational activity in mammalian cell nuclei (Nakamura et al., 1986; Nakayasu and Berezney, 1989; Berezny et al., 1995; Wei et al., 1998) are not understood. This lack of knowledge severely hinders a full understanding of the replication process in cell nuclei.

Furthermore, a variety of studies indicate that specific patterns of gene expression linked to particular functional states of the cell are related to a reorganization of chromatin domains (e.g., Brown et al., 1997; see also review by De Boni, 1994). Unraveling the mechanisms underlying these chromatin dynamics will be indispensable to understanding gene expression in the context of nuclear genome organization.

The present study describes a new quantitative 4D approach that contributes to an analysis of these basic biological and biophysical problems. The biological labeling techniques for studying these problems were developed only recently (Robinett et al., 1996; Shelby et al., 1996; Buchenau et al., 1997; Cardoso et al., 1997; Zink et al., 1998a; Marshall et al., 1997; Li et al., 1998; Zink et al., 1998a; Manders et al., 1999). It is still a challenge to perform 3D time-lapse studies in the range of several hours with fluorescently labeled live cells. For the evaluation of the 4D data sets obtained, sophisticated software tools are required to perform a reliable quantitative image analysis of the different types of motion possible. The present study describes an effort to combine the most recent developments from all of these different fields and thus prepares the ground for addressing more specific biological questions.

APPENDIX: TEST OF UNIFORMITY OF MOTION DIRECTIONS

Let

$$l_i = \sin\theta_i \cos\phi_i$$
$$m_i = \sin\theta_i \sin\phi_i$$
$$n_i = \cos\theta_i,$$
$$0 \le \theta_i \le \pi, \qquad 0 \le \phi_i < 2\pi \tag{A1}$$

be the direction cosines of motion of spot i, $i \in [0 \ldots N_{\text{spots}}]$ between sampling times t_1 and t_2.

The direction cosines are expressed in a direction matrix T, which holds the sums over the squared direction cosines of all spots:

$$T = \begin{bmatrix} \sum l_i^2 & \sum l_i m_i & \sum l_i n_i \\ \sum l_i m_i & \sum m_i^2 & \sum m_i n_i \\ \sum l_i n_i & \sum m_i n_i & \sum n_i^2 \end{bmatrix}, \tag{A2}$$

with eigenvalues τ_1, τ_2, τ_3, $\tau_1 + \tau_2 + \tau_3 = N_{\text{spots}}$. N_{spots} denotes the number of spots that were tracked from sampling times t_1 to t_2.

For an ideal uniform distribution of the directions,

$$\tau_1 = \tau_2 = \tau_3 = \frac{N_{\text{spots}}}{e} \tag{A3}$$

The test statistics for uniformity,

$$S_u = \frac{15}{2n} \sum_{i=1}^{3} \left(\tau_i - \frac{n}{3} \right)^2, \tag{A4}$$

are asymptotically distributed as χ_5^2 under the null hypothesis of uniformity (Bingham, 1964).

We thank Dr. E. H. K. Stelzer for providing access to the prototype of the Zeiss LSM 5 microscope and for kind help with the data acquisition. We are indebted to Prof. W. Ansorge for providing access to a microinjection apparatus, and to H. Luz for help with the data analysis. We are grateful to Dr. M. Hausmann for helpful discussions.

Financial support by the European Community (Biomed 2 program, BMH4-CT95-1139) and by the BMBF (German Human Genome Project, 01 KW 9620) is gratefully acknowledged.

REFERENCES

Berezney, R., M. J. Mortillaro, H. Ma, X. Wei, and J. Samarabandu. 1995. The nuclear matrix: a structural milieu for genomic function. *Int. Rev. Cytol.* 162A:1–65.

Bingham, C. 1964. Distributions on the sphere and on the projective plane. Ph.D. thesis. Yale University.

Bornfleth, H., P. Edelmann, D. Zink, and C. Cremer. 1999. Three-dimensional analysis of genome topology. *In*: Handbook of Computer Vision and Applications, Vol. III. B. Jähne, H. Haussecker, and P. Geissler, editors. Academic Press, San Diego and New York. 859–878.

Bornfleth, H., K. Sätzler, R. Eils, and C. Cremer. 1998. High-precision distance measurements and volume-conserving segmentation of objects near and below the resolution limit in three-dimensional confocal microscopy. *J. Microsc.* 189:118–136.

Brown, K. E., S. S. Guest, S. T. Smale, K. Hahm, M. Merkenschlager, and A. G. Fisher. 1997. Association of transcriptionally silent genes with Ikaros complexes at centromeric heterochromatin. *Cell.* 91:845–854.

Buchenau, P., H. Saumweber, and D. J. Arndt-Jovin. 1997. The dynamic nuclear redistribution of an hnRNP K-homologues protein during Dro-

sophila embryo development and heat shock. Flexibility of transcription sites in vivo. *J. Cell Biol.* 137:291–303.

Cardoso, M. C., C. Joseph, H. P. Rahn, R. Reusch, B. Nadal-Ginard, and H. Leonhardt. 1997. Mapping and use of a sequence that targets DNA ligase I to sites of DNA replication in vivo. *J. Cell Biol.* 139:579–587.

Cremer, T., C. Cremer, H. Baumann, C. K. Luedtke, K. Sperling, V. Teubner, and C. Zorn. 1982. Rabl's model of the interphase chromosome arrangement tested in Chinese hamster cells by premature chromosome condensation and laser-UV-microbeam experiments. *Hum. Genet.* 60:46–56.

Cremer, T., S. Dietzel, R. Eils, P. Lichter, and C. Cremer. 1995. Chromosome territories, nuclear matrix filaments and inter-chromatin channels: a topological view on nuclear architecture and function. *In* Kew Chromosome Conference IV. P. E. Brandham and M. D. Bennett, editors. Royal Botanic Gardens. 63–81.

Cremer, T., A. Kurz, R. Zirbel, S. Dietzel, B. Rinke, E. Schröck, M. R. Speicher, U. Mathieu, A. Jauch, P. Emmerich, and C. Cremer. 1993. Role of chromosome territories in the functional compartmentalisation of the cell nucleus. *Cold Spring Harb. Symp. Quant. Biol.* 58:777–792.

Cremer, C., C. Münkel, M. Granzow, A. Jauch, S. Dietzel, R. Eils, X. Y. Guan, P. S. Meltzer, J. M. Trent, J. Langowski, and T. Cremer. 1996. Nuclear architecture and the induction of chromosomal aberrations. *Mutat. Res.* 366:97–116.

De Boni, U. 1994. The interphase nucleus as a dynamic structure. *Int. Rev. Cytol.* 150:149–171.

Doolittle, K. W., I. Reddy, and J. G. McNally. 1995. 3D analysis of cell movement during normal and myosin-II-null cell morphogenesis in dictyostelium. *Dev. Biol.* 167:118–129.

Fauth, C. 1998. Evaluierung eines Verfahrens zur Darstellung von Chromosomen in lebenden Säugetierzellen. Diploma Thesis. Institut für Anthropologie und Humangenetik, LMU München.

Gelles, J., B. J. Schnapp, and M. P. Sheetz. 1988. Tracking kinesin-driven movements with nanometre-scale precision. *Nature.* 331:450–453.

Ghosh, R. N., and W. W. Webb. 1994. Automated detection and tracking of individual and clustered cell surface low density lipoprotein receptor molecules. *Biophys. J.* 66:1301–1318.

Gundersen, H. J., and Z. B. Jensen. 1987. The efficiency of systematic sampling in stereology and its prediction. *J. Microsc.* 147:229–263.

Hell, S., G. Reiner, C. Cremer, and E. H. K. Stelzer. 1993. Aberrations in confocal fluorescence microscopy induced by mismatches in refractive index. *J. Microsc.* 169:391–405.

Ingber, D. E. 1993. Cellular tensegrity: defining new rules of biological design that govern the cytoskeleton. *J. Cell Sci.* 104:613–627.

Jackson, D. A., and A. Pombo. 1998. Replicon clusters are stable units of chromosome structure: evidence that nuclear organization contributes to the efficient activation and propagation of S-phase in human cells. *J. Cell Biol.* 140:1285–1295.

Jähne, B. 1993. Digitale Bildverarbeitung. 3. Auflage. Springer-Verlag, Heidelberg, Berlin, and New York.

Lamond, A. I., and W. C. Earnshaw. 1998. Structure and function in the nucleus. *Science.* 280:547–553.

Landau, L. D., and E. M. Lifschitz. 1966. Lehrbuch der theoretischen Physik, Band VI, Sect. 59: Hydrodynamik. Akademie-Verlag, Berlin.

Li, G., G. Sudlow, and A. S. Belmont. 1998. Interphase cell cycle dynamics of a late-replicating, heterochromatic homogeneously staining region: precise choreography of condensation/decondensation and nuclear positioning. *J. Cell Biol.* 140:975–994.

Lindek, S., C. Cremer, and E. H. K. Stelzer. 1996. Confocal theta fluorescence microscopy with annular apertures. *Appl. Optics.* 35:126–130.

Manders, E. M., H. Kimura, and P. R. Cook. 1999. Direct imaging of DNA in living cells reveals the dynamics of chromosome formation. *J. Cell Biol.* 144:813–821.

Maniotis, A. J., C. S. Chen, and D. E. Ingber. 1997. Demonstration of mechanical connections between integrins, cytoskeletal filaments, and nucleoplasm that stabilize nuclear structure. *Proc. Natl. Acad. Sci. USA.* 49:849–854.

Mardia, K. V. 1972. Statistics of Directional Data. Academic Press, London.

Marshall, W. F., A. Straight, J. F. Marko, J. Swedlow, A. Dernburg, A. Belmont, A. W. Murray, D. A. Agard, and J. W. Sedat. 1997. Interphase chromosomes undergo constrained diffusional motion in living cells. *Curr. Biol.* 7:930–939.

Möbius, A. F. 1827. Der barycentrische Calcul—ein neues Hülfsmittel zur analytischen Behandlung der Geometrie. J. A. Barth, Leipzig.

Nakamura, H., T. Morita, and C. Sato. 1986. Structural organizations of replicon domains during DNA synthetic phase in the mammalian nucleus. *Exp. Cell Res.* 165:291–297.

Nakayasu, H. and R. Berezney. 1989. Mapping replicational sites in the eucaryotic cell nucleus. *J. Cell Biol.* 108:1–11.

Patwardhan, A. 1997. Subpixel position measurement using 1D, 2D and 3D centroid algorithms with emphasis on applications in confocal microscopy. *J. Microsc.* 186:246–257.

Qian, H., M. P. Sheetz, and E. L. Elson. 1991. Single particle tracking. Analysis of diffusion and flow in two-dimensional systems. *Biophys. J.* 60:910–921.

Robinett, C. C., A. Straight, G. Li, C. Willhelm, G. Sudlow, A. Murray, and A. S. Belmont. 1996. In vivo localization of DNA sequences and visualisation of large-scale chromatin organization using Lac operator/repressor recognition. *J. Cell Biol.* 135:1685–1700.

Saxton, M. J. 1993. Lateral diffusion in an archipelago (single particle diffusion). *Biophys. J.* 64:1766–1780.

Saxton, M. J. 1997. Single-particle tracking: the distribution of diffusion coefficients. *Biophys. J.* 72:1744–1753.

Schmidt, W. 1925. Gefügestatistik. *Tschermaks Mineralog. Petrographische Mitteilungen.* 38:392–423.

Shelby, R. D., K. M. Hahn, and K. F. Sullivan. 1996. Dynamic elastic behavior of α-satellite DNA domains visualized in situ in living human cells. *J. Cell Biol.* 135:545–557.

Sheppard, C. J. R., and P. Török. 1997. Effects of specimen refractive index on confocal imaging. *J. Microsc.* 185:366–374.

Sparvoi, F., C. Martin, A. Scienza, G. Gavazzi, and C. Tonelli. 1994. Cloning and molecular analysis of structural genes, involved inflavonoid and stilbene biosynthesis in grape (*Vitis vinifera* L.) *Plant Mol. Biol.* 24:743–755.

Verhaegh, N. A. M., and A. van Blaaderen. 1994. Dispersions of rhodamine-labeled silica spheres: synthesis, characterization, and fluorescence confocal scanning microscopy. *Langmuir.* 10:1427–1438.

Visser, A. E., R. Eils, A. Jauch, G. Little, T. Cremer, P. Bakker, and J. A. Aten. 1998. Spatial distribution of early and late replicating chromatin in interphase territories of active and inactive X-chromosomes. *Exp. Cell Res.* 243:398–407.

von Smoluchowski, M. 1917. Versuch einer mathematischen Theorie der Koagulationskinetik kolloider Lösungen. *Z. Phys. Chemie.* 92:129–168.

Wei, X., J. Samarabandu, R. S. Devdhar, A. J. Siegel, R. Acharya, and R. Berezney. 1998. Segregation of transcription and replication sites into higher order domains. *Science.* 281:1502–1505.

Yokota, H., G. van den Engh, J. E. Hearst, R. K. Sachs, and B. J. Trask. 1995. Evidence for the organization of chromatin in megabase pair-sized loops arranged along a random walk path in the human G0/G1 interphase nucleus. *J. Cell Biol.* 130:1239–1249.

Zink, D., H. Bornfleth, A. Visser, C. Cremer, and T. Cremer. 1999. The organisation of early and late replicating chromatin in human chromosome territories. *Exp. Cell Res.* 247:176–188.

Zink, D., and T. Cremer. 1998. Cell nucleus: chromosome dynamics in nuclei of living cells. *Curr. Biol.* 8:R321–R324.

Zink, D., T. Cremer, R. Saffrich, R. Fischer, M. F. Trendelenburg, W. Ansorge, and E. H. K. Stelzer. 1998. Structure and dynamics of human interphase chromosome territories in vivo. *Hum. Genet.* 102:241–251.